Computers and Geotechnics 178 (2025) 106898

Contents lists available at ScienceDirect

Computers and Geotechnics

journal homepage: www.elsevier.com/locate/compgeo

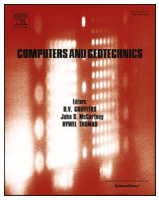

Research Paper

A numerical approach for CFD-DEM coupling method with pore network model considering the effect of anisotropic permeability in soil-rock mixtures

Zhilin Cao [a], Zhanping Song [a,b,*], Weichen Sun [c], Qiang Xie [c], Alessio Fumagalli [d,**], Xiaoxu Tian [b,e], XiaoLe Shen [b]

[a] Institute for Interdisciplinary and Innovation Research, Xi'an University of Architecture and Technology, Xi'an 710055, China
[b] School of Civil Engineering, Xi'an University of Architecture and Technology, Xi'an 710055, China
[c] School of Civil Engineering, Chongqing University, Chongqing 400044, China
[d] MOX Laboratory, Department of Mathematics, Politecnico di Milano, Milan 20133, Italy
[e] Shaanxi Key Laboratory of Geotechnical and Underground Space Engineering, Xi'an, 710055, China

ARTICLE INFO

Keywords:
Pore network model
DEM
Soil-rock mixture
Fluid-particle interaction
Particle loss

ABSTRACT

A new fluid–solid coupled numerical approach is developed by combining the CFD (Computational Fluid Dynamics) – DEM (discrete element method) with the pore network model (PNM) to simulate the erosion of the soil-rock mixture. The pore network with pore and pore pipes is constructed based on the particles and updated regularly. A relationship equation is derived between the permeability scalar for micro-scaled pore pipe and the anisotropic permeability tensor for macro-scaled fluid element. By the Delaunay-PorePy-PFC3D program framework, the erosion process of the soil-rock mixture with different fine contents (FCs) is simulated. The results show that the PNM-CFD-DEM model can meet the computational accuracy for simulating the rule-arranged uniform particles. The duration of the erosion stage is different for specimens with different FCs. The PNM-CFD-DEM model can reproduce the particle erosion paths in different specimens, as well as the adjustment of the pore network between their coarse particles. The preferential drag forces in the discrete portion take into account the pore network formed by the state of the particle buildup within each fluid element.

1. Introduction

A soil-rock mixture is a system of extremely heterogeneous geotechnical media formed since the Quaternary period, consisting of rock particles in sand, silt, clay, and others and much pore space, which is increasingly encountered in engineering construction (Medley, 1994; Xu, et al., 2009). Under the effect of rainfall or groundwater environmental infiltration, the soil-rock mixture is prone to erosion and loss of granular media, which can lead to landslides, avalanches, and other geologic hazards (Furtney et al., 2013; Wang et al., 2021). For example, dikes and dams are built over rivers and are typically constructed on soil-rock mixture foundations. During the flood season, internal erosion may occur in the dike or its foundation, which increases the risk of dam and dike failures (Jin et al., 2022); Unstable slopes with the soil-rock mixture are easily disrupted under sufficient water source conditions, and even directly transformed into soil-rock flow (Li et al., 2023; Nian et al., 2021); in underground engineering, the encountered sandy strata, fault broken zones, and severely weathered zones form a structural soil-rock mixture with poor stability and loose structure. Under high water pressure and excavation disturbance, the inrush water channels are formed, leading to chain disasters such as tunnel face collapse, formation collapse, and water and mud inrush disaster (Song et al., 2024; Xie et al., 2023).

Numerical simulation is an indispensable research tool for studying the fluid–solid coupling seepage failure process of soil-rock mixture. From the perspective of numerical computational scale, fluid–solid coupling computational methods can be categorized into two main groups: macroscopic and microscopic (Tsuji, 2007). Macroscale fluid–solid coupling model calculations treat a part of the geotechnical body and the flow field as a cell and act on each cell through Local Averaging

* Corresponding author at: Institute for Interdisciplinary and Innovation Research, Xi'an University of Architecture and Technology, Xi'an 710055, China.
** Corresponding author at: MOX Laboratory, Department of Mathematics, Politecnico di Milano, Milan 20133, Italy.
E-mail addresses: songzhpyt@xauat.edu.cn (Z. Song), alessio.fumagalli@polimi.it (A. Fumagalli).

https://doi.org/10.1016/j.compgeo.2024.106898
Received 3 June 2024; Received in revised form 11 October 2024; Accepted 4 November 2024
Available online 21 November 2024

Theory, also known as the continuous medium model. For the study of the seepage failure process of soil-rock mixture, many scholars are based on the finite element method (FEM), finite volume method (FVM), and finite difference method (FDM) and introduce medium porosity judgment criterion to analyze the seepage failure behavior during the formation process (Fleshman and Rice, 2014; Vandenboer et al., 2014). However, the macroscopic continuous medium model cannot consider the fine-grained migration, pore network structure redistribution, and other microscopic phenomena in the seepage failure process of soil-rock mixtures. The Discrete Element Method (DEM) has been widely applied to model granular materials for the microscale model. It has proven to be an effective tool for investigating granular materials' physics (Cui et al., 2016; Song et al., 2024; Song et al., 2024a). Since the 1970 s, Computational Fluid Dynamics (CFD) has also made tremendous progress and has been used to represent fluid evolution in fluid-particle systems (Anderson and Wendt, 1994; Wang et al., 2022). The particle–fluid coupled methods that compute particle motion by DEM and fluid motion by CFD were established, such as CFD-DEM (Kuang et al., 2020), SPH-DEM (Wu et al., 2016), LBM-DEM (Brumby et al., 2015), and so on. Among them, the coarse-grid CFD-DEM coupled method proposed by Tsuji et al. (Tsuji et al., 1993) is the most widely used in seepage damage (Wang et al., 2022). Hu et al. (Hu et al., 2020a; Z. Hu et al., 2020b, 2020c) used CFD-DEM to model suffusion and the undrained shear behavior of the eroded soils. Xu et al. (Xu et al., 2022) conducted to reproduce the constant head permeability tests of different rock-soil samples, and found that the Syamlal–O'Brien drag model of the CFD-DEM model leads to the accuracy in simulating sand permeability. Cao et al (Cao et al., 2022) constructed a CFD-DEM erosion model for soil-rock mixtures to reproduce the fine-grained erosion process and the change of fine particle skeleton force chain.

However, the coarse-grid CFD-DEM method is still based on the assumption of Local Averaging Theory in the macroscopic continuum approach, which quantifies the influence of solid particles on the seepage field based on the average porosity or permeability of each fluid element, which cannot accurately reflect the influence of the constantly changing pore network structure of the rock-soil mixtures on the fluid movement (Cheng et al., 2021). Some methods have been proposed to solve the problem of local averaging defects in the CFD-DEM method. For example, the CFD element is further refined, and the resolved CFD-DEM method was created, which requires a high resolution of the CFD fluid mesh or LBM lattice, i.e., The mesh or lattice size is required to be at least less than 1/8–1/10 of the particle diameter (Rettinger and Rüde, 2017; Solnordal et al., 2014). However, when the number of particles is large, the number of fluid elements or lattices in the coupled simulation is large, resulting in a large computational burden. So, the resolved method is only suitable for small-scale particle–fluid coupling simulations (Cheng, 2019). To balance computational efficiency, Cheng et al. (Cheng et al., 2021; Cheng et al., 2018). proposed a semi-solved CFD-DEM method based on the Fictitious Domain method in fine element technology for simulating the movement of fine particles in gap-graded soils caused by seepage. Catarano et al. (Catalano et al., 2013) adopted the pore network model (PNM) to couple the DEM and used the regular triangular and its dyadic Voronoi dissections to establish a pore space network of the rock. The flow pathways used to connect the pores are idealized as parallel-plate flow pipes at each DEM contact. The effect of the fluid on a given particle is simply the resultant force of the pressures of all the pores enclosing that particle. This approach is particularly effective in simulating the fracturing of rock under hydraulic pressure but faces challenges when dealing with large deformations of soil-rock mixtures during seepage failure (Wang et al., 2022). Zhang et al. (Zhang et al., 2020) introduced the dynamic Delaunay tetrahedral mesh technique to establish a DFM (Dynamic Fluid Mesh)-DEM model, in which the fluid mesh structure, permeability, and fluid-particle interaction forces are updated at predetermined intervals as the position of the coarse particles changes. This approach is effective in describing changes in particle distribution within gap-graded mixtures but is limited in other applications. These methods offer valuable insights for optimizing coarse-grid CFD-DEM approaches. However, they struggle to accurately depict the geometric structure and connectivity of pore pipes, particularly when addressing the anisotropic seepage characteristics of soil-rock mixtures and their evolution during seepage failure. Additionally, maintaining a balance between simulation accuracy and computational efficiency in representing the anisotropy of these mixtures remains a challenge.

In the present study, inspired by applying the pore network model (PNM) in optimizing CFD-DEM methods, a new PNM-CFD-DEM is proposed to study seepage failure and particle loss of soil-rock mixtures. A PNM based on the DEM particle is used to calculate the spatial distribution characteristics of pores and pore pipes between particles in each fluid element and to calculate the anisotropic permeability of each fluid element to optimize the local averaging interaction theory of the CFD-DEM method with porosity and average permeability. First, the calculated process of the anisotropic permeability of each fluid element based on PNM is described in Section 2. The numerical algorithm of the PNM-CFD-DEM coupling model is presented in Section 3, and the erosion process of three gap-graded soil-rock mixtures with different fine particle contents(FCs) was carried out in Section 4. Some discussion about the method is shown in Section 5. Finally, conclusions are drawn in Section 6 to summarize the contributions of this study.

2. Anisotropic permeability of each fluid element based on PNM

2.1. PNM based on DEM particles

From a microscopic view, the fluid and the solid occupy their respective areas during seepage, and the fluid flows through the tortuous pore pips. The pore pips' size, geometry, and extension direction affect the fluid flow (Song et al., 2024b; Fan et al., 2023; Hu et al., 2022). The spatial distribution of pore pips determines the anisotropy of seepage direction and the anisotropy permeability characteristics of porous media in a certain volume. The PNM of the soil-rock mixtures can simplify the pore structure into a combination of pores and pore pipes, as shown in Fig. 1. The voids in the pore structure are as pores, and the bonds between two neighboring pores are as pore pipes (Gao et al., 2012; Raoof and Hassanizadeh, 2009). The phenomenon of fluid seepage through a porous media is the flow of fluid through a pore network consisting of pores and pore pipes. For the construction of the PNM in the DEM particle model, this paper calculates the pore between particles by the Delaunay Tetrahedral Method and then calculates the pore pipes between different pores based on the distance between the pores and the radius of the pores, and finally completes the establishment of the PNM, as shown in Fig. 2.

(1) Delaunay tetrahedron mesh generating

Currently, the common methods for generating PNM include Delaunay triangulation, centered axial, and maximal sphere method (Hu et al., 2020a). This paper uses the most widely used Delaunay triangulation method for PNM. Delaunay triangulation considers all solid-phase particles in the PNM as representative points of their spherical or particle centers of mass (Gao, 2012; Steven et al., 1993). The Delaunay triangulation corresponding to the particle stack (Fig. 3 (a)) is shown in Fig. 3 (b).

As shown in Fig. 3, a seed triangle is selected by connecting the three centers of adjacent spheres. For each side of the seed triangle, sufficiently close sphere centroids are identified to form a near-regular tetrahedron based on the seed triangle. Until all the sphere centroids are traversed (Chan and Ng, 1988), a tetrahedral mesh model with the sphere centroids as nodes is built. Flattened tetrahedra are easily generated at the particle boundaries in the generated tetrahedra. Suppose a flattened tetrahedral is included in the subsequent calculations. In that case, the interior of the overly flattened tetrahedra will lead to a

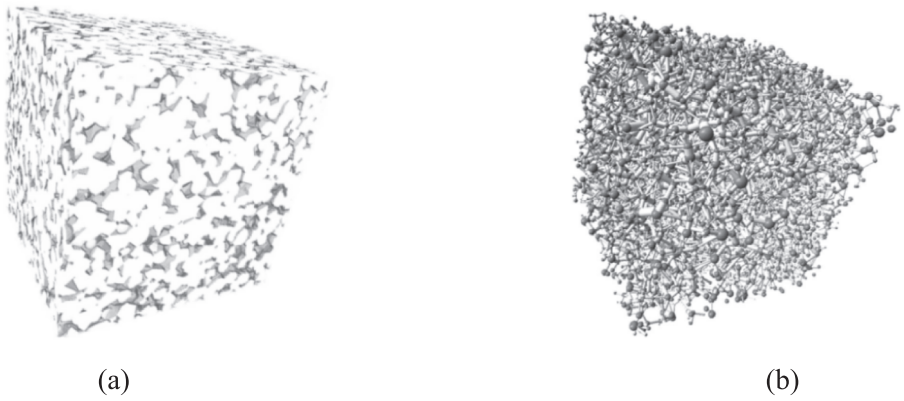

Fig. 1. PNM of porous media: (a) Three-dimensional visualization modeling of geotechnical bodies in porous media; (b) PNM in geotechnical bodies.

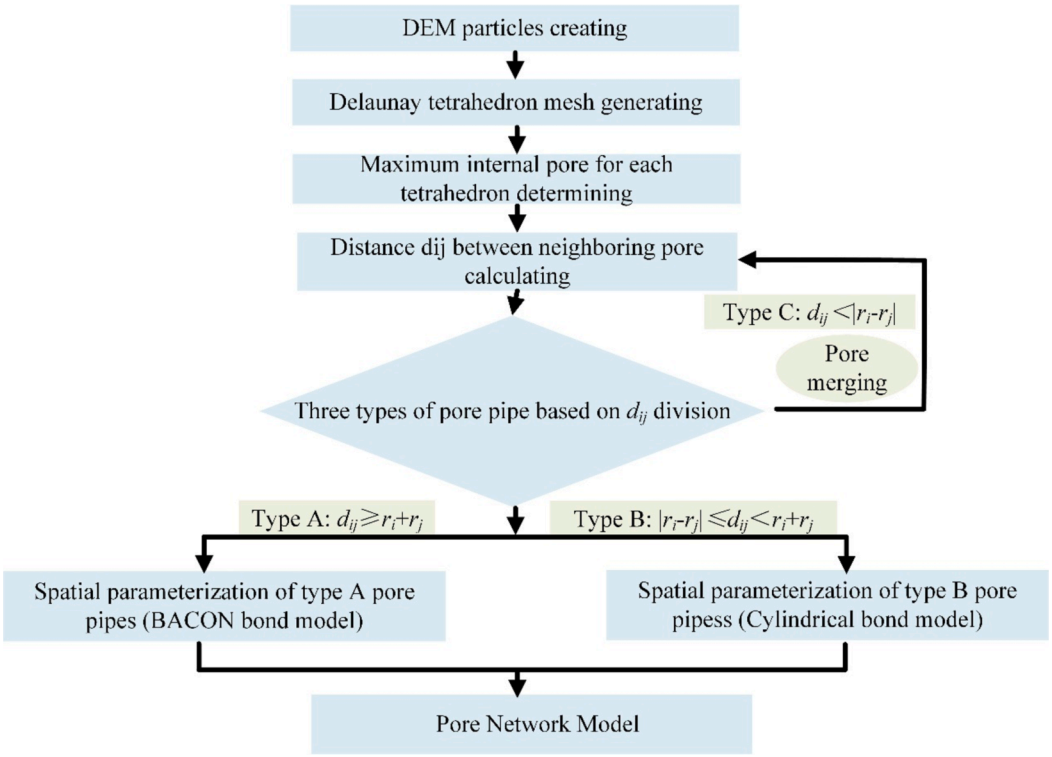

Fig. 2. PNM of DEM particles calculation procedure.

huge maximum of standard tangent spheres (pores), which does not match reality and leads to the failure of subsequent calculations to converge. In order to avoid the generated tetrahedra being too distorted, here we introduce the concept of sphericity coefficient to sieve the generated tetrahedra on the boundary (Wu et al., 2021), and the sphericity coefficients of the various tetrahedra are defined as the ratio of the tetrahedral surface area to the volume, which is calculated as follows:

$$\theta = \frac{4\pi\left(\frac{3V_p}{4\pi}\right)^{2/3}}{S_p} \tag{1}$$

where θ is the sphericity coefficient of the tetrahedron, the sphericity coefficient of the sphere is 1, and the sphericity coefficient of the orthotetrahedron is 0.671; V_p is the volume of the tetrahedron; S_p is the surface area of the tetrahedron. According to several attempts, the sphericity coefficient of 0.1 is taken as the threshold value, and the sphericity coefficient of the generated boundary tetrahedron is less than 0.1, which determines that the boundary-generated tetrahedron is too flat, and it is deleted or reclassified.

(2) Maximum internal pore for each tetrahedron determining

For the Delaunay tetrahedron, the ID of each tetrahedron, as well as the radius and coordinates of the four spheres located on the vertices of each tetrahedron, are recorded, and the indexes of each tetrahedron to the four neighboring tetrahedra are established. An iterative algorithm of the relevant system of nonlinear equations is introduced to obtain the center coordinates of the largest standard tangent pore ball inside each tetrahedron and its radius.

2.2. Pore pipes division and calculation

(1) Three types of pore pipe division

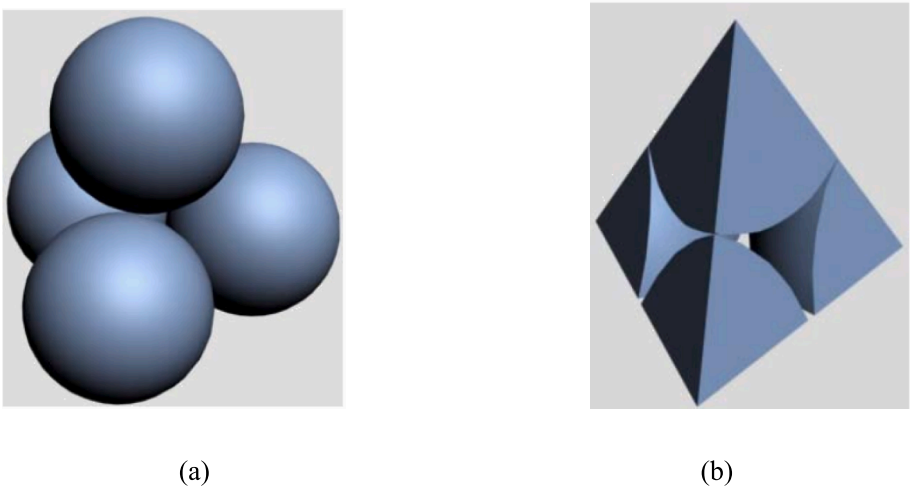

Fig. 3. Two views of one sample Delaunay cell: (a) Delaunay cell with four composing spheres; (b) Parts of spheres located inside the tetrahedron (Gao, 2012).

The pore space inside a Delaunay tetrahedron represents a pore. Each pore generated using the Delaunay tetrahedron method has four neighboring pores, and the corresponding pores share an identical triangular surface. Given two neighboring pores IDs as i and j, the corresponding pore ball radius are r_i and r_j, and d_{ij} is the distance between the centers of the two pores. Gao et al. (Gao, 2012) proposed three types of pore pip divisions based on the distances of the generated pores from each other. Type A pore pipe: two pores are separated ($d_{ij} \geq r_i + r_j$), as in Fig. 4 (a); Type B pore pipe: two pores intersect ($|r_i - r_j| \leq d_{ij} < r_i + r_j$), as in Fig. 4 (b); Type C pore pipe: the smaller radius pore ball is contained by the more giant radius ball ($d_{ij} < |r_i - r_j|$), as in Fig. 4 (c). The type C pore pipes are regarded as undirected, and it is necessary to merge these pores. The smaller radius pore needs incorporate into the larger radius pores, and to be re-calculated the distances between the neighboring pores and to be divided the pore pipes again until the type C pore pipes are no longer present.

(2) Spatial parameterization of pore pipes

The pore pipe undergoes convergence and contraction during the connection of each pore. Different distances between pores lead to the pore pipe's different locations and volume parameters. The following calculations are illustrated for the sites and volume space parameters of type A and B pore pipes.

Type A pore pipes: Existing studies have shown that the microstructural network of porous media can be better modeled by setting up convergent-divergent functionally derived bonds between mutually separated pores in porous media to connect neighboring pores (Ferziger et al., 2002; Mason, 1971). Acharya et al. (Acharya et al., 2004) argued that when the pore spacing is larger than the sum of the radius of the two-pore balls, the convergent-divergent functionally derived bond morphology of the pore pipes satisfies the Biconical abscissa Asymmetric CONcentric (BACON) bond. When a fluid passes through the pore pipe, and the ξ_F and ξ_G are the inlet and outlet of the BACON bond, respectively, as shown in Fig. 5.

The functions of the two ends of the BACON bond intersect at E (Fig. 5 (b)), and this position, ξ_E represents the smallest cross-sectional area of the pore pipe. The dimensionless functions $r(\xi)$ of the two ends of the ξ_F and ξ_G of the BACON bond can be expressed as follows:

$$r(\xi) = T_i(1-\xi)^n, \quad \xi_F \leq \xi \leq \xi_E \tag{2a}$$

$$r(\xi) = T_j\xi^n, \quad \xi_E \leq \xi \leq \xi_G \tag{2b}$$

where ξ characterizes any point in the distance between two pore balls and has a value from 0 to 1.

$$\xi = \frac{x}{d_{ij}}, 0 \leq x \leq d_{ij} \tag{3}$$

where x is the distance from the center of the pore ball to any point between the center points of adjacent holes.

T_i and T_j are both $r(\xi)$ values for the corresponding pores i and j:

$$T_{i(j)} = \frac{\overline{R}_{i(j)} sin(\frac{\pi}{\zeta})}{\left[1 - \overline{R}_{i(j)} cos(\frac{\pi}{\zeta})\right]^n} \tag{4}$$

where ζ is the coordination number in the two-dimensional plane, a pore ball may be connected to many neighboring pore balls, and the coordination number is generally between 3 and 10 (Acharya et al., 2004). In this paper, it is assumed that each pore ball is connected with four neighboring pore balls. The coordination number ζ is 4 and $\frac{\pi}{\zeta}$ is the BAF angle at Fig. 5(b), which represents the angle of the pore pipe at the

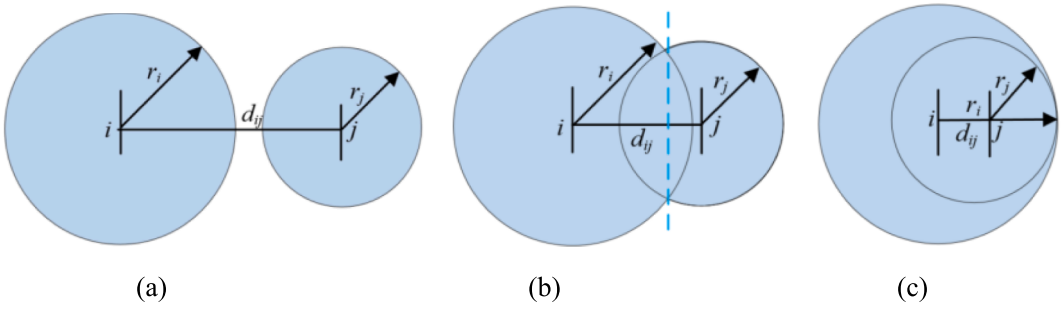

Fig. 4. Definitions of the three types of pore pipe: (a) Type A; (b) Type B; (c) Type C.

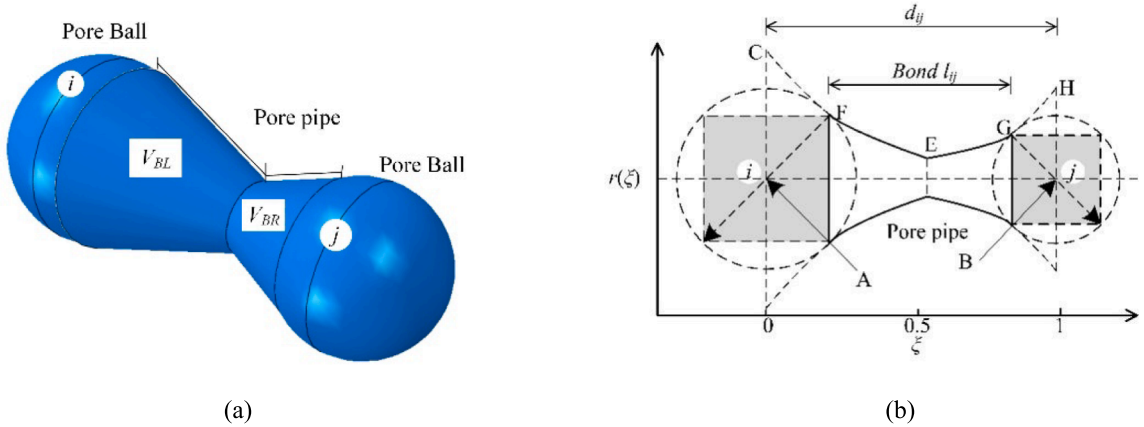

(a) (b)

Fig. 5. BACON bond of the type A pore pipe (Acharya et al., 2004): (a) 3D model; (b) Outline of the bond connecting two pore balls: pore ball i with radius r_i, and the center A at $\xi = 0$, and pore ball j with radius r_j and the center B at $\xi = 1$.

point of tangency to the pore ball.

n is a curvature parameter that determines the longitudinal shape and size of the BACON bond (Plessis, 1999). When the pore radius at both ends of the BACON bond is equal, $n = 0$. When the radius of the pores at the two ends of the BACON bond are not equal, $n > 0$. The dimensionless pore size $\overline{R}_{i(j)}$ is obtained by dimensionless processing of the pore sphere radius r_i and r_j based on the pore spacing d_{ij}:

$$\overline{R}_{i(j)} = \frac{r_{i(j)}}{d_{ij}},\ 0 < \overline{R}_{i(j)} \le 0.5 \tag{5}$$

The volume of type A pore pipe is the total volume $V_{BB-\mathrm{BACON}}$ as a function of the left and right ends of the BACON bond:

$$V_{BB-\mathrm{BACON}} = V_{BL} + V_{BR} \tag{6a}$$

$$V_{BL} = a_x d_{ij}^3 \int_{\xi_F}^{\xi_E} T_i^2 (1-\xi)^{2n} \mathrm{d}\xi \tag{6b}$$

$$V_{BR} = a_x d_{ij}^3 \int_{\xi_E}^{\xi_G} T_j^2 \xi^{2n} \mathrm{d}\xi \tag{6c}$$

where V_{BL} represents the volume at the left end of the BACON bond,$\xi_F \le \xi \le \xi_E$in Fig. 5(b), and V_{BR} represents the volume at the right end of the BACON bond, $\xi_E \le \xi \le \xi_G$in Fig. 5(b). a_x is the geometric shape factor. For a circular cross-section $a_x = \pi$ and for a square cross-section $a_x = 4$. This paper considers a circular cross-section as shown in Fig. 5 (a).

With the spatial coordinates (X_i, Y_i, Z_i) of the pore i, the spatial coordinates E_t of the pore pipe can be calculated:

$$E_t = (X_i, Y_i, Z_i) + \overrightarrow{l}_{ij} d_{ij} T_i^{\frac{1}{n}} \left(T_i^{\frac{1}{n}} + T_j^{\frac{1}{n}}\right)^{-1},\ n > 0 \tag{7a}$$

$$E_t = (X_i, Y_i, Z_i) + \overrightarrow{l}_{ij} d_{ij} \overline{R}_i (\overline{R}_i + \overline{R}_j)^{-1},\quad n = 0 \tag{7b}$$

where $\overrightarrow{l}_{ij}$ is the unit direction vector of the pore pipes $\overrightarrow{l}_{ij} = (X_i - X_j, Y_i - Y_j, Z_i - Z_j) \frac{1}{\sqrt{(X_i-X_j)^2+(Y_i-Y_j)^2+(Z_i-Z_j)^2}}$.

Type B pore pipes: As proposed by Gao (Gao, 2012), when two neighboring pores intersect, the flow direction between the pores is determined by using the intersecting region as the pore pipe (Fig. 6). The pore pipes are modeled as cylinders that connect the pores, where the cylinder's radius is equal to the radius of the common section between the two intersecting pore spheres (Fig. 6(a)). The length of the cylinder is set as 1/10 of the radius of the smaller of the two neighboring pore spheres.

As shown in Fig. 6(b), the radius of intersection of the pores can be obtained according to the Helen's volume equation $P = (r_i + r_j + d_{ij})/2$:

$$r_{ij} = 2\frac{\sqrt{P(P-r_i)(P-r_j)(P-d_{ij})}}{d_{ij}} \tag{8}$$

Then, the volume $V_{BB-\mathrm{cylinder}}$ of the cylinder bond of the type B pore pipe is:

$$V_{BB-\mathrm{cylinder}} = \frac{1}{10}\pi (r_{ij})^2 r_j \tag{9}$$

With the spatial coordinates (X_i, Y_i, Z_i) of the pore i, the spatial

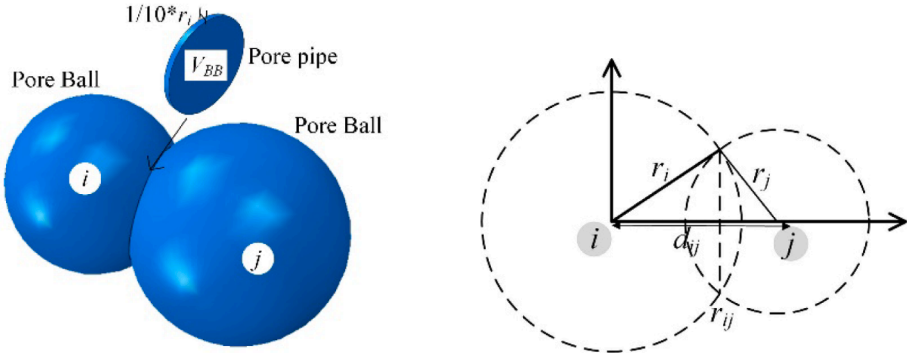

(a) (b)

Fig. 6. Cylinder bond of the type B pore pipe: (a) 3D model; (b) Outline of the bond connecting two pore balls: pore ball i with radius r_i, and pore ball j with radius r_j.

coordinates E_t of the pore pipe can be calculated:

$$E_t = (X_i, Y_i, Z_i) + \overrightarrow{l}_{ij}\sqrt{r_i^2 - r_{ij}{}^2} \tag{10}$$

2.3. Pore pipe discrimination of each fluid element

After completing the PNM, it is necessary to discriminate the generated pore pipes from the spatial regions of each fluid element. The Particle Centroid Method (Zhu and Yu, 2003) is selected for discriminating the pore pipes contained in each fluid element, as shown in Fig. 7. The spatial coordinates of the centroid of each pore pipe (throat for type A and centroid for type B pore pipe) are determined whether the center point of the pore pipe is within the fluid element.

However, it should be noted that the Particle Centroid Method does not distinguish between the volume of the pore pipes located inside and outside the fluid element, which can cause errors in the calculation of the pore volume, especially when the particle size is close to the element size, and this error cannot be ignored. In order to guarantee sufficient computational accuracy, the fluid elements should be divided finely enough to satisfy the calculation of fluid motion, and at the same time, a fluid element must contain a certain number of particles, which should satisfy the following inequality:

$$\frac{d_c}{\Delta x_{cfd}} > 5 \tag{11a}$$

$$\frac{\Delta x_{cfd}}{2r} > 3 \tag{11b}$$

where d_c is the minimum calculated width of the fluid domain; Δx_{cfd} is the calculated length of the fluid cell; r is the maximum particle size within the fluid element.

2.4. Anisotropic permeability of each fluid element

Assuming that the water movement within each pore pipe conforms to Darcy's law, the flow velocity v^p of a pore pipe can be calculated as:

$$v^p = \frac{-k}{\mu}\frac{(P_j - P_i)}{l^p} \tag{12}$$

where: l^p is the length of the pore pipe; k is the permeability of the pore pipe, which is considered to be the same for each pore pipe; and μ is the dynamic viscosity coefficient; $P_j and P_i$ are the pore water pressure at the entrance and exit of the pore pipe.

The macroscopic flow velocity $\langle v_i \rangle$ within each fluid element can be defined as:

$$\langle \overrightarrow{v} \rangle = \frac{1}{V_{BB_M}}\int \overrightarrow{v}^p dV_{BB} \tag{13a}$$

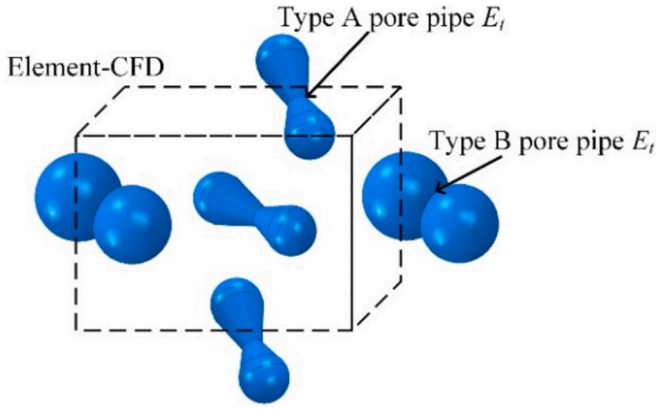

Fig. 7. Pore pipes discrimination of each fluid element.

$$V_{BB_M} = \sum V_{BB-\text{BACON}} + \sum V_{BB-\text{Cylinder}} \tag{13b}$$

where: $\overrightarrow{v}^p$ is the flow velocity along pore pipe p; V_{BB_M} is the total volume of M pore pipes within a fluid element. By simplifying the flow of pore pipes within the fluid element, this integration can be replaced by the sum of all M pore pipes contained in the fluid element volume V:

$$\langle \overrightarrow{v} \rangle_M = \frac{1}{V_{BB_M}}\sum_{p=1}^{M} \overrightarrow{v}^p V_{BB}^p \tag{14}$$

where: V_{BB}^p is the volume of the pore pipe; V_{BB} is the total volume of pore pipes within one fluid element.

And the flow velocity inside the different pore pipes, which is related to the velocity v^p of the water flow in addition to the unit vector n_i^p of the pore pipe, can be expressed as

$$\overrightarrow{v}^p = v^p n_i^p \tag{15}$$

Bringing Eq. (15) into Eq. (12), the flow velocities in different pore pipes can be calculated as:

$$\overrightarrow{v}^p = -\frac{-k}{\mu}\frac{\Delta P n_i^p}{l^p} \tag{16}$$

where: ΔP is the pressure difference between the entrance and exit of the pore pipe. Assuming that the average pressure gradient $\frac{\partial P}{\partial x_j}$ within the fluid element is applicable to the pressure level within each pore pipe, then the pressure gradient ΔP can be calculated as:

$$\Delta P = l^p n_j^p \frac{\partial P}{\partial x_j} \tag{17}$$

By substituting Eqs. (16) and (17) into Eq. (14), the macroscopic flow velocity $\langle \overrightarrow{v} \rangle_M$ of the fluid element can be calculated as:

$$\langle \overrightarrow{v} \rangle_M = \left[-\frac{1}{V_{BB_M}}\sum_{p=1}^{M} \frac{k}{\mu} n_i^p n_j^p V_{BB}^p \right] \frac{\partial P}{\partial x_j} \tag{18}$$

By comparing this expression with the macroscopic Darcy's law, it can be shown that the permeability tensor of a fluid element can be expressed as:

$$k_{ij} = \frac{1}{V_{BB_M}}\sum_{p=1}^{M} k n_i^p n_j^p V_{BB}^p \tag{19}$$

For the existing CFD-DEM fluid–solid coupling methods, a fluid element is considered as an isotropically permeable material, the permeability is the average permeability $\bar{k}$ and can be calculated as:

$$\begin{aligned}\bar{k} &= \frac{1}{3}(k_{xx} + k_{yy} + k_{zz}) = \frac{k}{3V_{BB_M}}\sum_{p=1}^{M} V_{BB}^p \left[(n_x^p)^2 + \left(n_y^p\right)^2 + (n_z^p)^2 \right] \\ &= \frac{k}{3V_{BB_M}}\sum_{p=1}^{M} V_{BB}^p \end{aligned} \tag{20}$$

So, the permeability k of pore pipes can be calculated as:

$$k = \frac{3V_{BB_M}}{\sum_{p=1}^{M} V_{BB}^p}\bar{k} \tag{21}$$

Then the macroscopic permeability tensor k_{ij} of a fluid element can be expressed by the average permeability $\bar{k}$ as:

$$k_{ij}=\begin{bmatrix} k_{xx} & k_{xy} & k_{xz} \\ k_{yx} & k_{yy} & k_{yz} \\ k_{zx} & k_{zy} & k_{zz} \end{bmatrix} = \frac{3}{\sum_{p=1}^{M} V_{BB}^{p}} \begin{bmatrix} \sum_{p=1}^{M} (n_x^p)^2 V_{BB}^p & \sum_{p=1}^{M} n_x^p n_y^p V_{BB}^p & \sum_{p=1}^{M} n_x^p n_z^p V_{BB}^p \\ \sum_{p=1}^{M} n_y^p n_x^p V_{BB}^p & \sum_{p=1}^{M} (n_y^p)^2 V_{BB}^p & \sum_{p=1}^{M} n_y^p n_z^p V_{BB}^p \\ \sum_{p=1}^{M} n_z^p n_x^p V_{BB}^p & \sum_{p=1}^{M} n_z^p n_y^p V_{BB}^p & \sum_{p=1}^{M} (n_z^p)^2 V_{BB}^p \end{bmatrix} \bar{k} \tag{22}$$

From Eq. (22), the permeability tensor based on the pore network distribution can characterize the anisotropic permeability of porous media within the fluid element in different directions, which can more accurately calculate the flow and transport phenomena in the porous media. What is more, the permeability tensor can reflect the permeability differences in different directions, which in turn can better consider the fluid-particle interactions inside the porous medium. In porous media, permeability differences in different directions can lead to different drag forces on particles within a fluid element in different directions.

3. Numerical algorithm of PNM-CFD-DEM coupling model

3.1. Governing equations

(1) Particle phase

The behavior of the particle phase is controlled by Newton's law of motion, and the governing equations of the particle phase are shown in Eqs (23) and (24) (Wang et al., 2022):

$$\frac{\partial \vec{u}}{\partial t}=\frac{\vec{f}_{mesh}+\vec{f}_{fluid}}{m_p}+\vec{g} \tag{23}$$

$$\frac{\partial \vec{\omega}}{\partial t}=\frac{\vec{M}_p}{I_p} \tag{24}$$

where $\vec{u}$ is the particle velocity, t is the numerical calculation time, $\vec{f}_{fluid}$ is the total force applied by the fluid on the particle, m_p is the particle mass, $\vec{f}_{mesh}$ is the sum of additional forces (externally applied forces and contact forces) acting on the particle, $\vec{g}$ is the acceleration due to gravity, $\vec{\omega}$ is the particle's angular velocity, I_p is the moment of inertia, and $\vec{M}_p$ is the moment acting on the particle.

(2) Fluid phase with anisotropic permeability

The relationship between each fluid element's porosity and average permeability was established through the Kozeny-Carman (K-C) equation (Valdecir et al., 2021). Considering the anisotropic permeability of each fluid element based on PNM, the fluid phase equations based on Darcy's law are as follows:

$$\vec{v}=-\frac{k_{ij}}{\mu}\vec{\nabla}p \tag{25a}$$

$$\nabla \bullet \vec{v}=0 \tag{25b}$$

$$k_{ij}=\frac{3\bar{k}(\varphi_t)}{\sum_{p=1}^{M} V_{BB}^p}\sum_{p=1}^{M} n_i^{pipe} n_j^{pipe} V_{BB}^p \tag{25c}$$

$$\bar{k}(\varphi_t)=\begin{cases} \dfrac{1}{180}\dfrac{\varphi_t^3}{(1-\varphi_t)^2}(2r_e)^2 & \varphi_t \le 0.7 \\ \bar{k}(0.7) & \varphi_t > 0.7 \end{cases} \tag{25d}$$

where $\bar{k}(\varphi_t)$ is the macroscopic average permeability as a function of the porosity of the fluid element; r_e is the average radius of the particles; φ_t is the porosity that is continuously updated with coupling time. The upper limit of porosity of 0.7 is taken. When the porosity of the fluid element exceeds 0.7, most particles in the fluid element are washed away. Above 0.7 porosity, the permeability coefficient is taken as a fixed value.

(3) Fluid-Particle interaction force

The fluid-particle interaction force consists of three components: the fluid drag force, $\vec{f}_{drag}$, the force induced by the fluid pressure gradient, $\frac{4}{3}\pi r^3\vec{\nabla}p$, and the fluid buoyancy force on the particles, $\frac{4}{3}\pi r^3\rho_f\vec{g}$, as follows (Itasca Consulting Group I, 2020; Tsuji et al., 1993):

$$\vec{f}_{fluid}=\vec{f}_{drag}+\frac{4}{3}\pi r^3(\vec{\nabla}p-\rho_f\vec{g}) \tag{26}$$

The drag force $\vec{f}_{drag}$ is defined as

$$\vec{f}_{drag}=\vec{f}_0\varphi_t^{-\chi} \tag{27}$$

where $\vec{f}_0$ is the single-particle drag force, and φ_t is the porosity of the fluid element in which the particle resides. The χ term is an empirical factor to account for the local porosity. This correction term makes the force applied to both high- and low-porosity systems and for a large range of Reynolds numbers (Felice et al, 1994)

$$\vec{f}_0=\frac{1}{2}C_d\rho_f\pi r^2|\vec{u}-\vec{v}|(\vec{u}-\vec{v}) \tag{28}$$

where C_d is the drag coefficient, ρ_f is the fluid density, r is the particle radius, $\vec{v}$ is the fluid velocity, and $\vec{u}$ is the particle velocity. The drag coefficient is defined as

$$C_d=\left(0.63+\frac{4.8}{\sqrt{Re_p}}\right)^2 \tag{29}$$

where Re_p is the particle Reynolds number.

The empirical coefficient χ is defined as:

$$\chi=3.7-0.65exp\left(-\frac{(1.5-\log_{10}Re_p)^2}{2}\right) \tag{30}$$

The particle Reynolds number is

$$Re_p=\frac{2\rho_f r|\vec{u}-\vec{v}|}{\mu_f} \tag{31}$$

where μ_f is the fluid viscosity.

3.2. Numerical implementation of PNM-CFD-DEM coupling

For the PNM-CFD-DEM coupling model, the PNM is built by the Delaunay data library (Scipy.Spatial.Delaunay), and the Taichi library (https://taichi-lang.cn), which supports GPU parallel computing engine technology, is introduced to improve the computational efficiency of particle discrimination; the seepage field of the geotechnical body is calculated by the porous media seepage simulation open source software PorePy (Keilegavlen et al., 2021), and the PyGeoN data library (https://github.com/compgeo-mox/pygeon) is introduced to convert the flow velocity from surface to the center of each fluid element of hybrid virtual finite method (VFM) in the PorePy solver; the DEM particle motion is

calculated by the commercial software PFC3D. Through the Itasca data library (https://github.com/jkfurtney/itasca-python), which has a complete set of transmission control protocols (TCP), the direct interaction of the information of seepage field with anisotropic permeability and particle motion is realized in Windows computer operating system and Python language environment.

The Delaunay- PorePy- PFC3D workflow of the PNM-CFD-DEM coupling model is shown in Fig. 8. Firstly, the DEM model is set up, and the fluid element is generated according to the particle boundary. Subsequently, the PNM of the DEM model is built based on the location of all the particles, pore pipes are discriminated within each fluid element, and then the anisotropic permeability tensor within each fluid element is calculated based on pore pipes and the average permeability of each fluid element. An incompressible fluid is assumed, and Darcy's law is used to calculate the local flow velocity and pore pressure. A fluid-particle interaction force is applied to each particle, and the process repeats. The pore pipes, anisotropic permeability tensor, and flow force are updated at predetermined intervals. When the total number of steps reaches a predetermined limit, the server PFC3D software will first automatically shut down, and then the client PorePy software will automatically shut down.

3.3. Validation based on Rule-arranged uniform particles

A classic example in the PFC software documentation (Itasca Consulting Group I., 2020; Cao et al., 2022; Xie et al., 2023) was used to prove the correctness of the PNM-CFD-DEM model and the stability of the Delaunay – PorePy- PFC3D coupling computational program. A granular material is contained in a rectangular box with dimensions 0.1 m by 0.2 m by 0.1 m. Water flows into the box perpendicular to the x-z plan at y = 0 at 1e-5 m^3/s. The walls of the box are impermeable except for the inlet and a 2 cm by 2 cm outlet in the box on the y = 0.2 plane, where the pressure is held constant. The particles making up the

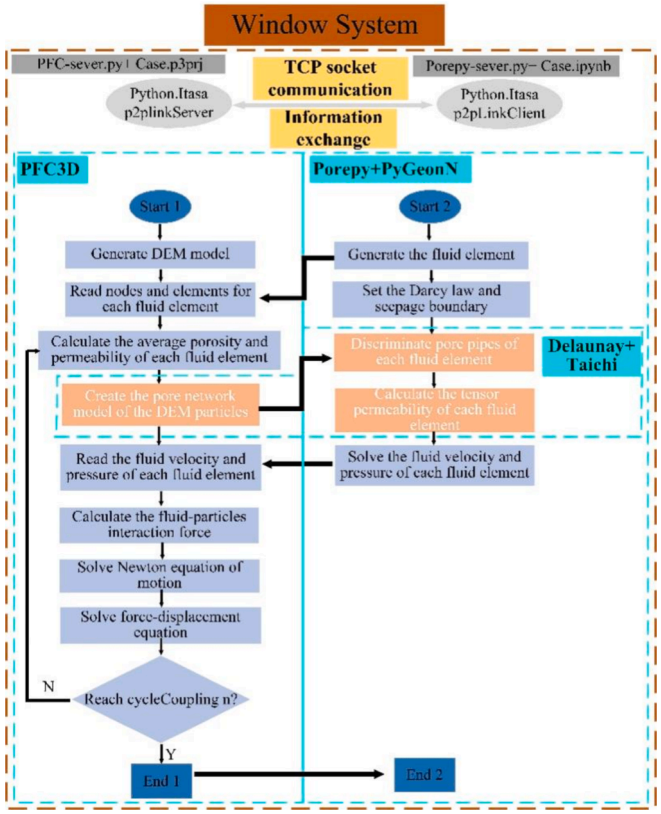

Fig. 8. Workflow of PNM-CFD-DEM coupling simulation.

granular material have an average radius of 0.0025 m and a density of 2600 kg/m^3. No gravitational forces are applied. Friction is not considered for contact between particles and wall elements. The flow accelerates as it converges on the outlet surface. The particles are displaced through the outlet surface, as shown in Fig. 9 (a).

As shown in Fig. 9 (b), the total number of particles is 16,000, each fluid element is a cube with a side length of 0.01 m, the total number of elements is 2,000, and each fluid element contains 16 particles, which can be calculated as the porosity within each fluid element is 0.476. Because the particles are uniformly and regularly arranged with the same permeation channels in the X, Y, and Z directions, it can be regarded as an isotropic material. Two fluid–solid coupling models and two coupling program frameworks are used to calculate the particle loss model numerically. The first method adopts the traditional CFD-DEM coupling model in the computational cases in the PFC3D user manual (Itasca Consulting Group I, 2018), which is implemented using the FiPy-PFC3D coupling framework, and the seepage equations of motion adopt Darcy's law with average permeability and K-C equations in the classical solution Eqs. (25a) and (25d); the second method still uses the traditional CFD-DEM coupling model but is implemented using the PorePy-PFC3D coupling framework; the third method uses the PNM-CFD-DEM coupling model, which is implemented using the Delaunay-PorePy-PFC3D coupling framework. All three methods use the above boundary conditions and flow-solid parameters, and the results of particle displacement field, fluid velocity field, and fluid pressure field calculations for the three calculation methods under the same calculation boundary and physical time are compared, as shown in Table 1.

From Table 1, comparing the overall distribution patterns of the maximum values of flow velocity and pressure in the results of the two fluid–solid coupling models, the numerical results are basically the same, which is due to the uniform regular arrangement of particles, the permeability in the X, Y, and Z directions within each fluid element are the same, and the anisotropic permeability tensor of the PNM-CFD-DEM model are the same as the average permeability of the CFD-DEM model. However, the relative error of the particle displacement distribution in the results of the three calculation methods is relatively larger. This may be because the displacement of the particles is determined by the cumulative motion of the particles in the DEM simulation. In each step of the calculation, the accumulation of resistance and pressure differences leads to a gradual deviation of the displacement. Although the relative differences in flow velocity and pressure are small, their cumulative effect is more significant in the calculation of particle displacement. What is more, the PNM-CFD-DEM model generates and updates the pore network by Delaunay triangular mesh. In the region close to the outlet, the local pore structure changes under the fluid acceleration and particle loss, resulting in a change in the direction of the fluid–structure coupling force. The conventional CFD-DEM model lags behind this change and fails to accurately capture the change in the local seepage direction, which leads to a deviation in the results of the two models. In addition, the fluid pressure calculations in PorePy have been applied to many projects to ensure their accuracy(Keilegavlen et al., 2021). The PNM-CFD-DEM model with the Delaunay-PorePy-PFC3D coupling program framework can meet the computational accuracy.

4. Suffusion in gap-graded rock-soil mixtures

4.1. Model setup

A numerical experiment is conducted to simulate the suffusion of gap-graded rock-soil mixtures by coupling the PNM-CFD-DEM method. In this study, a cylindrical specimen 50 mm in diameter and 125 mm in height is generated, containing a gap-graded geotechnical mixture (Fig. 10). The lower wall is removed and a perforated diaphragm with a circular hole (7 mm diameter) and spacing of 10 mm is placed. A rolling resistance linear model which incorporates a torque acting on the contacting pieces to counteract rolling motion is employed to simulate the

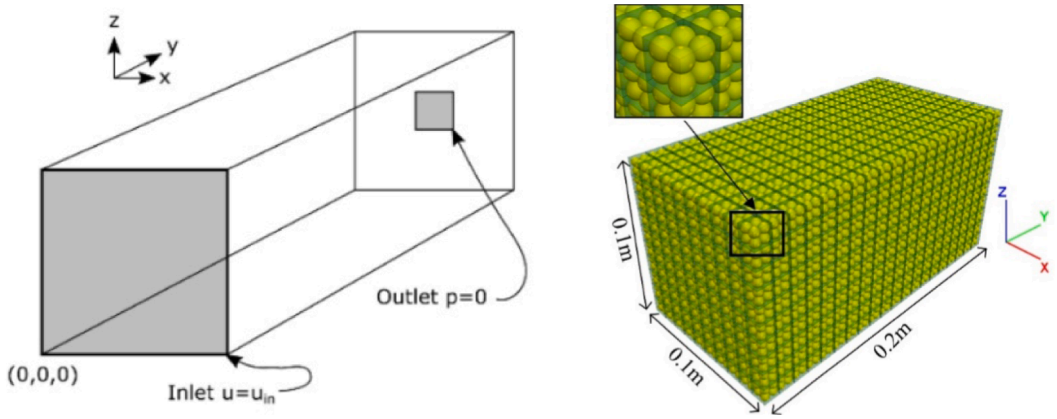

Fig. 9. Regularly arranged particle loss model: (a) schematic of problem geometry; (b) numerical modeling.

Table 1
Comparison of the test results of the three methods.

Field	CFD-DEM model in FiPy-PFC3D program	CFD-DEM model in the PorePy-PFC3D program	*Error*	PNM-CFD-DEM model in the Delaunay-PorePy-PFC3D program	*Error*
Displacement (m)	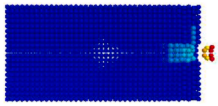	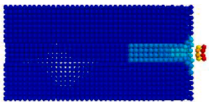	10.04 %	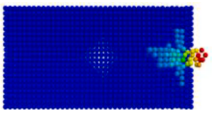	9.99 %
Velocity (m/s)	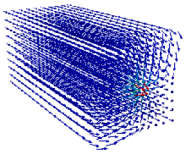	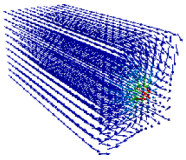	−0.0098 %	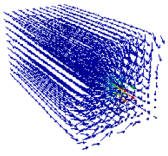	4.35 %
Pressure (Pa)	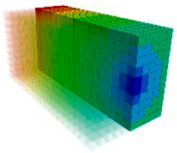	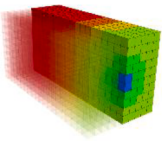	4.23 %	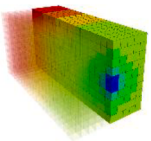	3.19 %

Note: (1) The maximum relative error, *Er* is based on the calculation result of the first method (the result of the demonstration case in the manual). Take the maximum displacement maximum relative error of the second PorePy-PFC3D model and the first FiPy-PFC3D model as an example: $Er = \frac{D_1 - D_2}{D_2} * 100\%$, where D_1 is the maximum displacement of the calculation result of the FiPy-PFC3D model, and D_2 is the maximum displacement of the calculation result of the PorePy-PFC3D model; (2) The particle displacement field is the X = 0.005 m profile.

soil contacts. The input parameters are shown in Table 2 according to (Cao et al., 2022). In the specimen, the diameter of coarse particles is on average 6 times larger than that of the fine particles. The diameter of the coarse particle is uniformly distributed between 8–10 mm, and the diameter of the fine particle is uniformly distributed between 1–2 mm. The specimens with FCs = 20 %, 30 %, and 40 % are modeled, as shown in Fig. 10. The confining stress that is applied on the particles on the top and lateral sample surfaces (effective stress) is 0.1 kPa. All particle

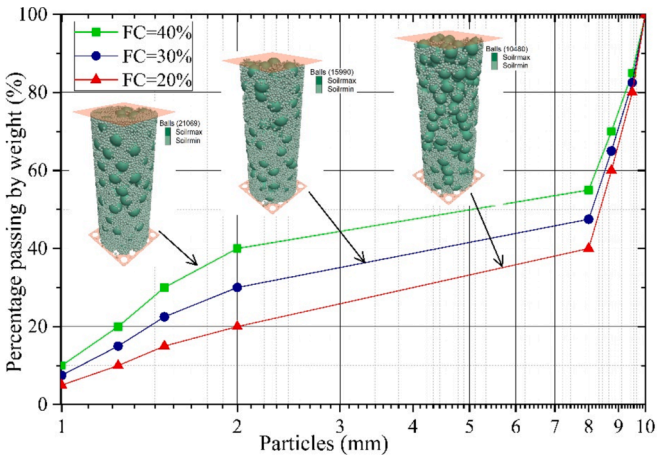

Fig. 10. Particle size distributions for the numerical specimens with different FCs.

Table 2
Calculation parameters of the PFC3D model (Cao et al., 2022).

Parameter	Value	
	Particle	Wall
Particle density (kg/m^3)	2630	–
Effective modulus (Pa)	1.5e8	1.0e9
Normal-to-shear stiffness ratio	1.0	1.00
Contact friction coefficient	0.5	0.01
Normal critical damping ratio	0.2	0.20
Shear critical damping ratio	0.2	0.20
Rolling resistance coefficient	0.1	0.10
Time step (s)	1e-7	–

information (including position, velocity, and drag force), contact forces, and energies within the samples were recorded every 0.1 s during each suffusion simulation, with a total duration of 50 s, as shown in Table 3. The calculation was conducted on a computer with Intel I9-9900 K and 32 GB RAM.

The fluid enters from the top of the model and outflows from the bottom. The pressure gradient was set to 0.4. For the gap-graded particle erosion, the large pores formed between coarse particles are used as pore network construction in this study. The erosion of fine particles is considered as migration between the large pores formed between the coarse particles. The centroids of coarse particles and contact points of coarse particles-walls are used to generate PNM. Taking the specimen with FC = 40 % as an example, the initial fluid velocity and pressure in each element, and drag force in each particle are shown in Fig. 11 (a), (b), and (c), respectively. Influenced by the PNM, the fluid velocity and drag force of the different fluid elements change and do not only seep from top to bottom along the pressure gradient.

4.2. Transportation of fine particles

The total mass of fine particles removed by erosion is monitored

Table 3
Calculation parameters during the coupling process.

Parameter	Value
Fluid density (kg/m^3)	1e3
Fluid dynamic viscosity (Pa·s)	1e-3
Gravitational acceleration (m/s^2)	9.8
DEM timestep (s)	1e-7
Coupling interval (s)	0.1
CFD update interval	20
Total simulation time (s)	50

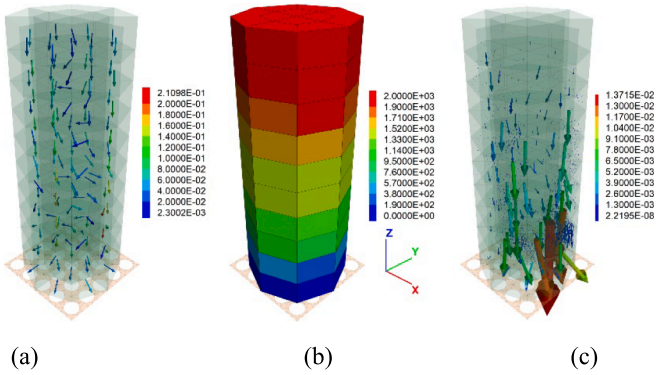

Fig. 11. (a) Initial flow velocity at the beginning of the numerical modeling (m/s), (b) Initial pressure (Pa), (c) Initial drag force of particles (N).

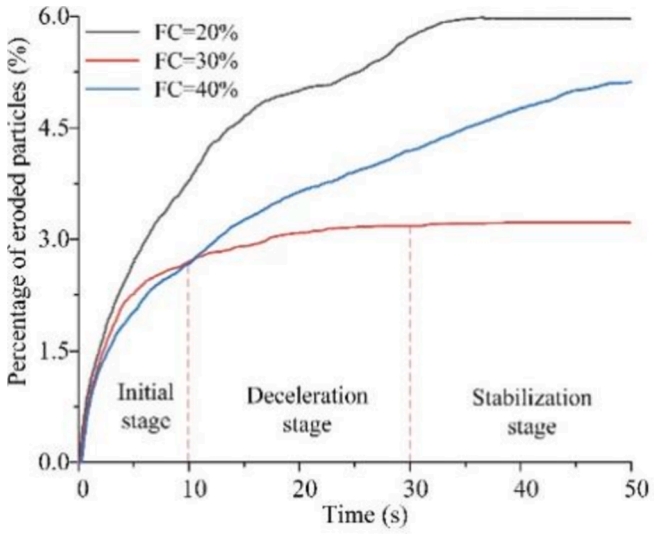

Fig. 12. Cumulative eroded particle percentage at different times of different FCs.

(Fig. 12). The evolution of the internal erosion can be divided into three stages according to the variation of erosion rate, i.e. initial rapid stage, deceleration stage, and stabilization stage. In the initial stage, large quantities of particles are carried away by gravity and water flow. In the deceleration stage, the erosion rate slows down gradually. In the stabilization stage, the erosion process tends to stop. The shape of the erosion curve agrees well with the results of laboratory erosion experiments (Bendahmane et al., 2008). Fine particle migration during different erosion stages was selected for further analysis. Fig. 13 depicts the internal migration of particles in the presorted 6-layer at different times. Fig. 14 shows the homogenized cloud plot of the movement velocity of the fine particles at 5 s. Rapid erosion occurs for specimens with different FCs, and the pattern of fine particle erosion is different for different heights, influenced by the structure of the pore network formed by coarse particles.

For the specimen with FC = 20 %, the rapid erosion stage is roughly 0–30 s, and particles of different heights are migrating and eroding out of the specimen, resulting in the highest erosion rate (Fig. 12), with particles of different heights moving at larger velocities (Fig. 13(a)). For the specimen with FC = 30 %, this skeletal structure is the most stable with the lowest erosion rate and the duration of the three phases of erosion is the most pronounced. The rapid erosion stage is roughly 0–10 s, in the first rapid erosion stage, the first layer of particles at the top of the specimen migrates downward, gradually lost, the middle layer of fine particles has formed an obvious erosion channel, the particle

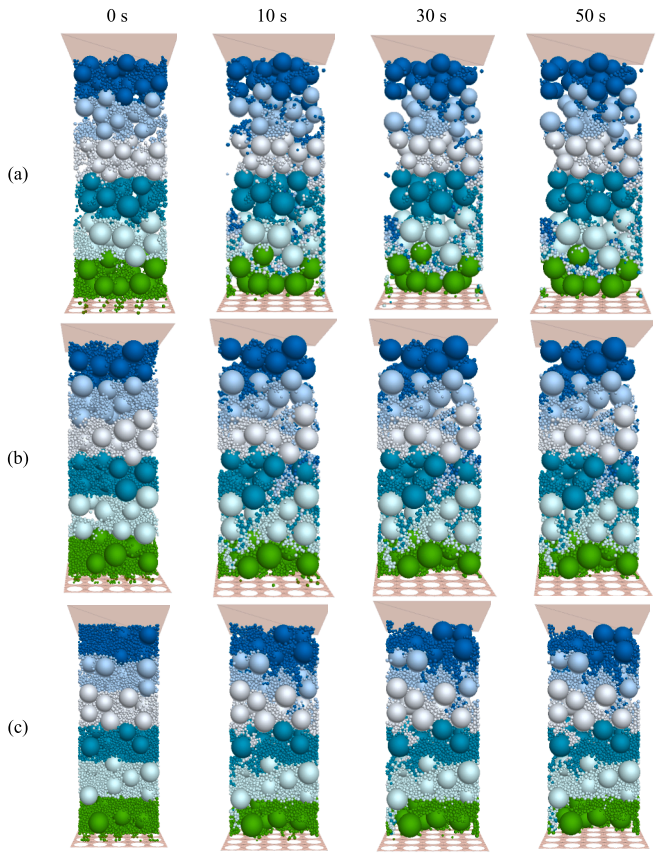

Fig. 13. Migration of particles in each layer of samples. (a) FC = 20 %; (b) FC = 30 %; (c) FC = 40 %.

velocity in the erosion channel is more prominent (Fig. 14(b)). For the sample with FC = 40 %, the initial rapid erosion stage lasts the longest, roughly 0——46 s. Although the content of fine particles is the largest, the fine particles fill the pores between the coarse particles, resulting in fewer particles in the upper 1st to 4th layers of particles being eroded out of the sample, and in the 5 s of the rapid erosion stage by the effect of the complete filling of the fine particles in the coarse particles, the fine particles have the lowest velocity of movement.

4.3. Drag force on the fine particles

In real granular fluid systems with gap-graded particles, the migration behavior of fine particles is influenced by the pore network formed between coarse particles (Cheng et al., 2021; Cheng et al., 2018), as shown in Fig. 14(b). In the PNM-CFD-DEM method, the effect of the pore network between coarse particles on the seepage field is considered, and in turn, the variation of the preferential drag force in the dominant seepage channel between the particles and the fluid is captured. In order to further investigate the effect of drag force on fine particle migration, the drag forces on three fine particle sizes (1.0 mm, 1.5 mm, and 2.0 mm) in different specimens were selected and statistically analyzed as shown in Fig. 15. Overall, it is seen that the larger the particle size, the higher the drag force suffered in different FCs. For the specimen with FC = 20 %, with the loss of fine particles, the fine particles with a diameter of 2.0 mm were subjected to a more discrete distribution of drag force, and some particles were subjected to a drag force 1–1.5 times that of the others (Fig. 15(b)), which represented that they were subjected to the preferential flow formed by the intermittently graded particles; for the specimen with FC = 30 %, the degree of discretization in the distribution of drag force was less than that of the specimen with FC = 20 %, and the drag force is essentially unchanged during the erosion deceleration stage (Fig. 15(c) and (d)). For the specimen with FC = 40 %, which is subjected to fine particles sufficiently filling the pore network between coarse particles, the drag force they are subjected to is essentially continuously distributed.

4.4. Micro-behavior: Coordination number and Pore network

The macroscopic manifestation is caused by internal erosion, which is mainly caused by micro-mechanical behavior at the particle scale. As the erosion process develops, the stacking state between coarse and fine particles is constantly changing, and the corresponding pore network between coarse particles is also changing. The contact state between individual particles in a sample can be expressed in terms of the average contact number per particle (Farahnak et al., 2013). This is referred to as the coordination number and is calculated using the following formula:

$$Z = 2\frac{N_c}{N_p} \tag{32}$$

where the coordination number Z is the average number of contacts per particle, which quantifies the number of contacts per particle in the material and is a measure of packing density or packing strength at the particle scale(Farahnak et al., 2013); N_c is the total number of contacts and N_p is the number of particles. Particles in a mixture can only participate in stress transfer in a load-bearing structure if the number of contacts between one particle and other particles (coarse, fine, wall) is greater than 3. That is, the average number of contacts per particle in the zone (Z) is greater than or equal to 3.

Fig. 16 shows the variation of coordination number with time at different heights. Fig. 17 shows the pore network between coarse

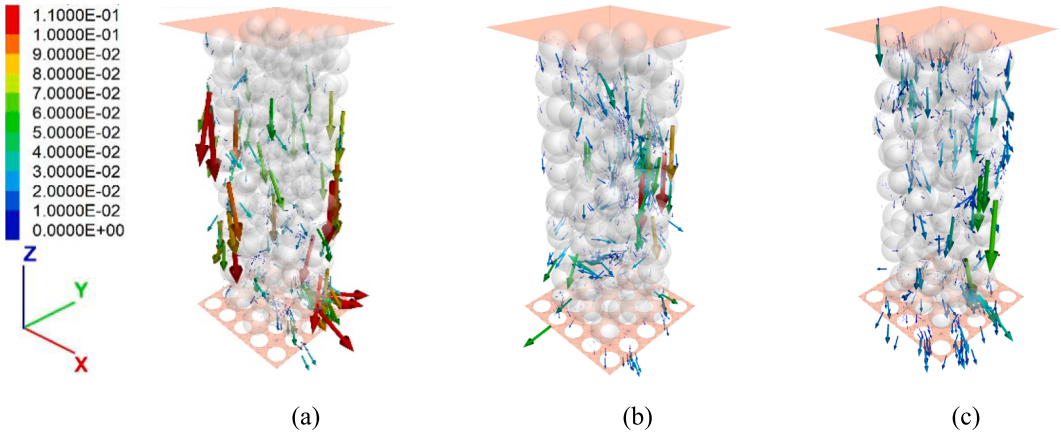

Fig. 14. Homogenized cloud plot of the movement velocity of the fine particles at 5 s: (a) FC = 20 %; (b) FC = 30 %; (b) FC = 40 %.

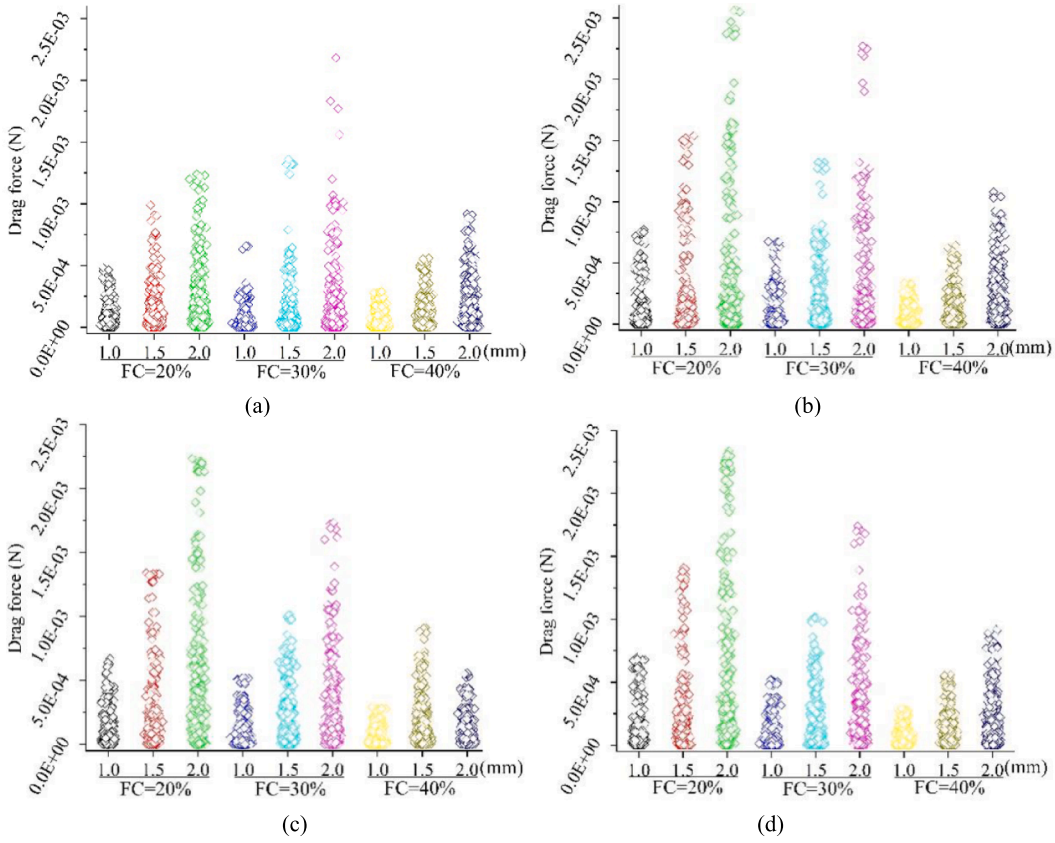

Fig. 15. Distributions of drag forces on fine particles at different times of different FCs: (a) 0.1 s; (b) 5 s; (c) 25 s; (d) 50 s.

particles at different times. The smaller the coordination number, the less stable the load-bearing skeleton structure is. Overall, the coordination number was the smallest in the bottom lossy zone (6th layer), followed by the top lossy zone (1st layer), and then the middle lossy zone (2nd to 5th layers). Except for the bottom loss region in the specimen with FC = 40 %, the average number of contacts between particles increased with the passage of fine particles, and the overall skeletal structure and pore network were further stabilized. In the specimen with FC = 20 %, due to more coarse particles, more pores and pore pipes were formed between the coarse particles (Fig. 17(a)), and the loss of fine particles in all layers resulted in large fluctuations in the coordination number changes at different heights, and the pore network between coarse particles was adjusted until it reached the stabilization stage where the coordination number changes were stabilized. In the specimen with FC = 30 %, the coordination number and pore network were in the rapid erosion stage for 10 s and then basically stabilized without change (Fig. 17(b)). In the specimen with FC = 40 %, the overall coordination number was initially higher due to the filling of the pore network formed by the coarse particles with the fine particles. As can be seen from the pore network formed by the coarse particles, the pore network changes very little (Fig. 17(c)). The loss zone at the bottom is in an unstable state (coordination number less than 2.5). With the loss of unstable fine particles, the coordination number gradually increases until it reaches about 3.0.

5. Discussion about the PNM-CFD-DEM model

Internal erosion mechanisms are related to the FCs under high hydraulic pressure (Kenney and Lau, 2011; Skempton and Brogan, 1994). When the FC is 20 % and the coarse particles form the stressed skeleton

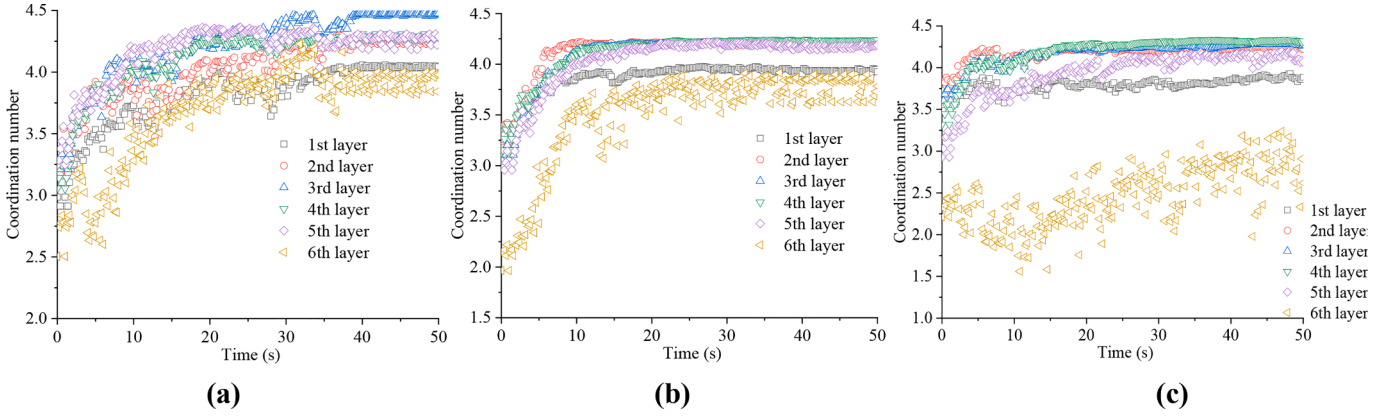

Fig. 16. Coordination number at different heights: (a) FC = 20 %; (b) FC = 30 %; (c) FC = 40 %.

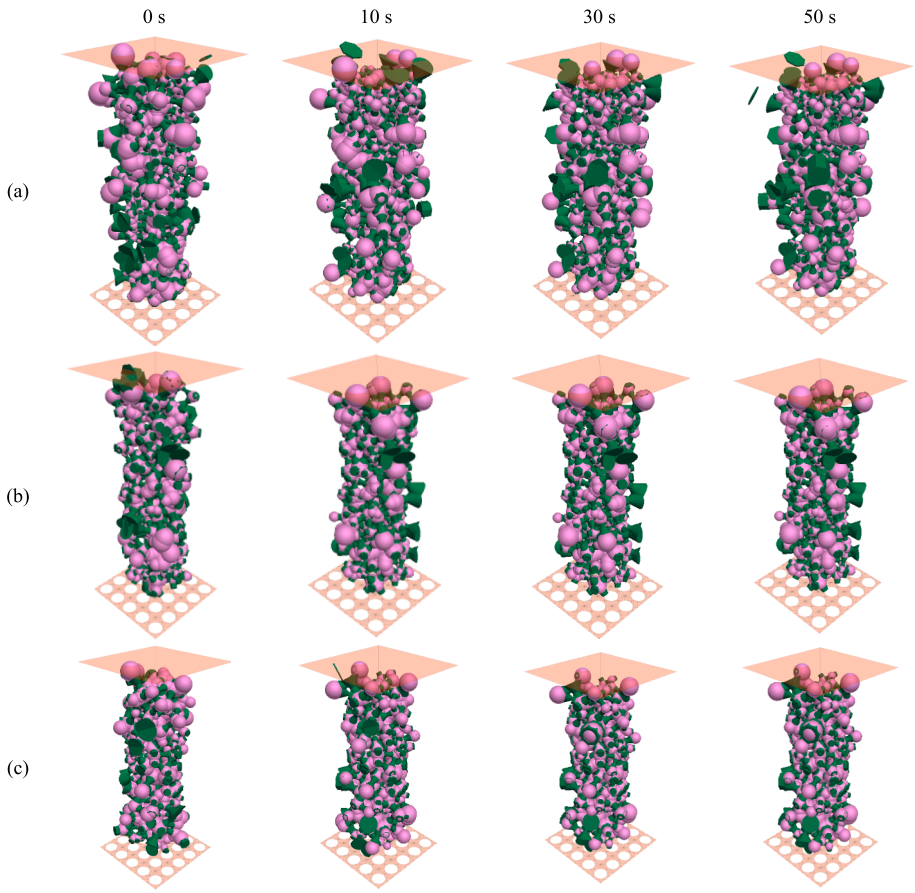

Fig. 17. Pore network at different times: (a) FC = 20 %; (b) FC = 30 %; (c) FC = 40 % (note: Pore balls with diameters larger than 8 mm are not shown, which are mainly generated by the contact between the particles and the outer wall.).

(Minh et al., 2014), the fine particles at different heights in the soil-rock mixture migrate with the fluid through the pore spaces between the coarse particles under vertical infiltration and gravity, which progressively manifests a great dragging force (Fig. 14(b)) and ultimately the high erosion rate (Fig. 12). When the FC is 30 %, despite the dominant seepage channel formed by the pore between coarse particles (Fig. 13b), it is gradually stabilized and the erosion rate is the lowest (Fig. 12), and the pore network completes the adjustment rapidly. When the FC is 40 %, the fine particles fill into the coarse particles and the load transfer effect of the mixture (contributed by the fine particles) becomes large (Thevanayagam et al., 2002; Vallejo, 2001). Affected by the loss of fine particles, the pore network has been adjusting, albeit very slightly, and has not been affected by the more discrete and extremely large drag forces.

In the unresolved CFD-DEM fluid–solid coupling method, the effect of the intrinsic heterogeneity of the gap-graded soil-rock mixture on the fluid flow is largely masked by the over-averaging of domains with sizes larger than the diameter of the coarse particles. Preferential flow and great drag forces on certain fine particles will not be captured (Cheng et al., 2021; Cheng et al., 2018). The advantage of the PNM-CFD-DEM model is that the seepage field can be corrected to simulate the preferential drag forces in the discrete portion by taking into account the pore network formed by the state of the particle buildup within each fluid element (Fig. 14). Visual representation of pore network changes in soil-rock mixtures during erosion. This new model is suitable for calculating soil-rock mixtures with anisotropic seepage characteristics, reproducing the differences in erosion caused by the loss of particles from the interior. It is worth noting that the semi-unresolved CFD-DEM method proposed by Cheng et al. (Cheng et al., 2021; Cheng et al., 2018) addresses the shortcomings of the local averaging assumption of the conventional CFD-DEM model by refining the pore-scale flow field around coarse particles. However, its computational time is at least 144 times that of the CFD-DEM model, while the computational time of the PNM-CFD-DEM model is about 4–5 times that of the CFD-DEM model. Therefore, the PNM-CFD-DEM model can be applied to model geotechnical mixtures on a larger scale. It has to be said that the PNM-CFD-DEM model may not be able to achieve the level of accuracy of the semi-unresolved CFD-DEM when simulating the complex flow behavior around coarse particles. In addition, for the motion of material or soil particles in water with insignificant anisotropy (sparse flow conditions), the PNM-CFD-DEM method may not offer significant advantages over the conventional CFD-DEM method, thus reducing the need for application in these cases.

6. Conclusions

In this study, a new numerical method for fluid–solid coupling is developed by combining CFD-DEM with pore network modeling (PNM). This study demonstrates the method to reveal the anisotropic seepage characteristics of soil-rock mixtures. A pore network with pores and pore pipes was constructed based on particles and updated periodically. A relationship equation between the fine-scale pore pipe permeability scalar and the macroscopic anisotropic permeability tensor was derived. The numerical scheme takes into account the anisotropic permeability changes due to pore pipe variations.

In order to implement the PNM-CFD-DEM method numerically, a new framework, Delaunay – PorePy – PFC3D, is also developed. The erosion process of three gap-graded soil-rock mixtures with FCs was simulated. The erosion process can be divided into a rapid erosion stage, a decelerated erosion stage, and a stabilization stage. The rapid erosion

stage is the longest when the FC = 40 %, followed by the specimen with FC = 20 %. The specimen with FC = 30 %, which has the longest erosion time, reaches stabilization the fastest. Influenced by the pore network constituted by coarse particles, in the specimen with FC = 20 %, particles flowed out of the pores between coarse particles at different heights; in the specimen with FC = 30 %, coarse and fine particles together constituted the structure, and there existed a clear dominant erosion channel; and in the specimen with FC = 40 %, influenced by fine particles filling in the pore space between coarse particles, the pore network, although changing, changed less, and only a significant amount of erosion occurs at the very bottom.

The PNM-CFD-DEM model can reproduce the particle erosion paths of the different specimens, as well as the adjustment of the pore network between the coarse particles. The flow direction within the fluid cells is corrected by the permeability tensor built based on the pore network so that the flow direction of each fluid cell can reflect the fine-scale seepage pipeline of the particles within each fluid cell in real-time, which leads to a more reasonable value and direction of the drag force of the fluid-particle interaction. The adjustment of the pore network during the erosion of the soil-rock mixture can be visualized in real-time.

CRediT authorship contribution statement

Zhilin Cao: Writing – original draft, Visualization, Supervision, Software, Formal analysis, Data curation, Conceptualization. **Zhanping Song:** Resources, Funding acquisition, Conceptualization. **Weichen Sun:** Software, Methodology. **Qiang Xie:** Methodology, Conceptualization. **Alessio Fumagalli:** Software, Methodology, Data curation. **Xiaoxu Tian:** Validation, Data curation. **XiaoLe Shen:** Visualization, Methodology.

Declaration of competing interest

The authors declare that they have no known competing financial interests or personal relationships that could have appeared to influence the work reported in this paper.

Acknowledgments

This work is partially supported by the National Natural Science Foundation of China (No. 52178393) and the Shaanxi Province Innovation Capability Support Program - Innovation Team (2020TD-005).

Data availability

Data will be made available on request.

References

Acharya, R.C., Sjoerd, E.A.T.M., Anton, L., 2004. Porosity–permeability properties generated with a new 2-parameter 3D hydraulic pore-network model for consolidated and unconsolidated porous media. Adv. Water Resour. 27 (7), 707–723.
Anderson, J.D., Wendt, J., 1994. Computational fluid dynamics. Springer.
Bendahmane, F., Marot, D., Alexis, A., 2008. Experimental Parametric Study of Suffusion and Backward Erosion. J. Geotech. Geoenviron. Eng. 134 (1), 57–67.
Brumby, P.E., Sato, T., Nagao, J., Tenma, N., Narita, H., 2015. Coupled LBM–DEM Micro-scale Simulations of Cohesive Particle Erosion Due to Shear Flows. Transp. Porous Media 109 (1), 43–60.
Cao, Z.L., Sun, W.C., Xie, Q., Wu, Z.H., Fu, X., Fumagalli, A., Tian, D.L., Liang, L., 2022. Fluid–solid coupled model for the internal erosion of gap-graded soil–rock mixtures with different fines contents: Its verification and application. Hydrol. Process. 36 (9), e14677.
Catalano, E., Chareyre, B., Barthélémy, E., 2013. Pore-scale modeling of fluid-particles interaction and emerging poromechanical effects. Int. J. Numer. Anal. Meth. Geomech. 38 (1), 51–71.
Chan, S.K., Ng, K.M., 1988. Geometrical characteristics of the pore space in a random packing of equal spheres. Powder Technol. 54 (2), 147–155.
Cheng, K., 2019. Study on DEM-based Numerical Methods for Seepage-induced Fine Particle Migration in Gap-graded Soils. Dalian University of Technology, Dalian, China.
Cheng, K., Wang, Y., Yang, Q., 2018. A semi-resolved CFD-DEM model for seepage-induced fine particle migration in gap-graded soils. Comput. Geotech. 100, 30–51.
Cheng, K., Zhang, C.Y., Peng, K.R., Liu, H.S., Ahmad, M., 2021. Un-resolved CFD-DEM method: An insight into its limitations in the modelling of suffusion in gap-graded soils. Powder Technol. 381 (1), 520–538.
Cui, Y.F., Nouri, A., Chan, D., Rahmati, E., 2016. A new approach to DEM simulation of sand production. J. Pet. Sci. Eng. 147, 56–67.
Fan, S.Y., Song, Z.P., Li, X., Tian, X.X., Liu, L.B.C., Li, K.L., 2023. Theoretical analysis and verification of the influence of bubble, pore throat and water film on pore water seepage characteristics-taking sandstone as the research object. Arch. Civ. Mech. Eng. 23 (4), 225.
Farahnak, L.M., Soroush, A., Tabatabaie, S.P., Shafipour, R., 2013. Stress transmission in internally unstable gap-graded soils using discrete element modeling. Powder Technol. 47, 161–171.
Felice, R.D., De, F.R., 1994. The voidage function for fluid-particle interaction systems. Int. J. Multiph. Flow 20 (1), 153–159.
Ferziger, J.H., Perić, M., Street, R.L., 2002. Computational methods for fluid dynamics. Springer.
Fleshman, M.S., Rice, J.D., 2014. Laboratory modeling of the mechanisms of piping erosion initiation. J. Geotech. Geoenviron. Eng. 140 (6), 04014017.
Furtney, J., Zhang, F., Han, Y., 2013. Review of methods and applications for incorporating fluid flow in the Discrete Element Method. ©2013 Itasca International Inc. Minneapolis. 2013, 1–10.
Gao, S.Y., 2012. Micromechanical study of two-phase flow during air sparging. New Jersey Institute of Technology, State of New Jersey, America.
Gao, S., Meegoda, J.N., Hu, L., 2012. Two methods for pore network of porous media. Int. J. Numer. Anal. Meth. Geomech. 36 (18), 1954–1970.
Hu, L.M., Lin, D.T., Zhang, P.W., Zhang, X.H., Guo, H.H., Jay, N.M., Dong, X.Q., 2022. Pore structure model for porous media and application in seepage analysis. Journal of Taiyuan University of Technology. 53 (03), 360–370.
Hu, Y.Q., Wang, Q., Zhao, J.Z., Xie, S.C., Jiang, H., 2020a. A Novel porous media permeability model based on fractal theory and ideal particle pore-space geometry assumption. Energies 13 (3), 510.
Hu, Z., Yang, Z.X., Zhang, Y.D., 2020b. CFD-DEM modeling of suffusion effect on undrained behavior of internally unstable soils. Comput. Geotech. 126, 103692.
Hu, Z., Zhang, Y., Yang, Z., 2020c. Suffusion-induced evolution of mechanical and microstructural properties of gap-graded soils using CFD-DEM. J. Geotech. Geoenviron. Eng. 146 (5), 04020024.
Itasca Consulting Group I., 2020. PFC6.0 Documentation. Minneapolis: Itasca Consulting Group Inc.
Jin, W., Deng, Z.Z., Wang, G., Zhang, D., Wei, L.Y., 2022. Internal erosion experiments on sandy gravel alluvium in an embankment dam foundation emphasizing horizontal seepage and high surcharge pressure. Water. 14 (20), 3285.
Keilegavlen, E., Berge, R., Fumagalli, A., Berre, I., 2021. PorePy: an open-source software for simulation of multiphysics processes in fractured porous media. Comput. Geosci. 25 (1), 243–265.
Kenney, T.C., Lau, D., 2011. Internal stability of granular filters: Reply. Can. Geotech. J. 22 (2), 215–225.
Kuang, S., Zhou, M., Yu, A., 2020. CFD-DEM modelling and simulation of pneumatic conveying: A review. Powder Technol. 365, 186–207.
Li, D.Y., Nian, T.K., Tiong, R.L.K., Shen, Y.Q., Shao, Z., 2023. River blockage and impulse wave evolution of the Baige landslide in October 2018: Insights from coupled DEM-CFD analyses. Eng. Geol. 321, 107169.
Mason, G., 1971. A model of the pore space in a random packing of equal spheres. J. Colloid Interface Sci. 35 (2), 279–287.
Medley, E.W., 1994. The engineering characterization of melanges and similar block-in-matrix rocks (Bimrocks). University of California, Berkeley, America.
Minh, N.H., Cheng, Y.P., 2014. Thornton C. Strong force networks in granular mixtures. Granul. Matter 16 (1), 69–78.
Nian, T.K., Wu, H., Takara, K., Li, D.Y., Zhang, Y.J., 2021. Numerical investigation on the evolution of landslide-induced river blocking using coupled DEM-CFD. Comput. Geotech. 134, 104101.
Plessis, J.P.D., 1999. Introducing a percolation threshold in pore-scale modelling. Phys. Chem. Earth Part A. 24 (7), 617–620.
Raoof, A., Hassanizadeh, S.M., 2009. A New method for generating pore-network models of porous media. Transp. Porous Media 81 (3), 391–407.
Rettinger, C., Rüde, U., 2017. A comparative study of fluid-particle coupling methods for fully resolved lattice Boltzmann simulations. Comput. Fluids 154, 74–89.
Skempton, A.W., Brogan, J.M., 1994. Experiments on piping in sandy gravels. Géotechnique. 44 (3), 449–460.
Solnordal, C., Witt, P., Prakash, M., Liovic, P., Hager, A., Kloss, C., Pirker, S., Goniva, C., 2014. Parallel resolved open source CFD-DEM: Method, Validation, and Application. Journal of Computational Multiphase Flows 6 (1), 13–27.
Song, Z.P., Li, X., Fan, S.Y., Shen, X.L., Wang, K.S., Zhang, M.N., Pu, J.Y., 2024b. Mesoscopic analysis of creep characteristics of hard tuff considering damage. Arch. Civ. Mech. Eng. 24 (2), 72.
Song, Y.Q., Zhang, D.C., Ranjith, P.G., Zhou, Z.Q., Wu, B.L., Kong, L., Chen, L.X., Huang, J.C., 2024a. A comprehensive study of fines migration in internally unstable natural gas hydrate reservoirs. Powder Technol. 433, 119193.
Steven, L., Bryant, P.R.K., David, W.M., 1993. Network Model Evaluation of Permeability and Spatial Correlation in a Real Random Sphere Packing. Transp. Porous Media 11, 53–70.
Thevanayagam, S., Shenthan, T., Mohan, S., Liang, J., 2002. Undrained Fragility of Clean Sands, Silty Sands, and Sandy Silts. J. Geotech. Geoenviron. Eng. 128 (10), 849–859.
Tsuji, Y., 2007. Multi-scale modeling of dense phase gas-particle flow. Chem. Eng. Sci. 62 (13), 3410–3418.

Tsuji, Y., Kawaguchi, T., Tanaka, T., 1993. Discrete particle simulation of two-dimensional fluidized bed. Powder Technol. 77 (1), 79–87.
Valdecir, A.S., Antônio, F.S., Tatiana, A.S., Gustavo, P.O., 2021. Poiseuille-Number-Based Kozeny-Carman model for computation of pore shape factors on arbitrary cross sections. Transp. Porous Media 138 (1), 99–131.
Vallejo, L.E., 2001. Interpretation of the limits in shear strength in binary granular mixtures. Can. Geotech. J. 38 (5), 1097–1104.
Vandenboer, K., Beek, V.V., Bezuijen, A., 2014. 3D finite element method (FEM) simulation of groundwater flow during backward erosion piping. Front. Struct. Civ. Eng. 8 (2), 160–166.
Wang, X.K., Tang, Y., Huang, B., Hu, T.T., Ling, D.S., 2021. Review on numerical simulation of the internal soil erosion mechanisms using the discrete element method. Water. 13 (2), 169.
Wang, T., Zhang, F.S., Furtney, J., Damjanac, B., 2022. A review of methods, applications, and limitations for incorporating fluid flow in the discrete element method. J. Rock Mech. Geotech. Eng. 4 (3), 1005–1024.
Wu, K., Yang, D., Wright, N., 2016. A coupled SPH-DEM model for fluid-structure interaction problems with free-surface flow and structural failure. Comput. Struct. 177, 141–161.
Wu, K., Sun, W.C., Liu, S.Y., Cai, G.J., 2021. Influence of particle shape on the shear behavior of superellipsoids by discrete element method in 3D. Adv. Powder Technol. 32 (11), 4017–4029.
Xie, Q., Cao, Z.L., Sun, W.C., Fumagalli, A., Fu, X., Wu, Z.H., Wu, K., 2023. Numerical simulation of the fluid-solid coupling mechanism of water and mud inrush in a water-rich fault tunnel. Tunn. Undergr. Space Technol. 131, 104796.
Xu, W.J., Hu, R.L., 2009. Conception, classification, and significations of soil-rock mixture. Hydrogeology & Engineering Geology. 36 (04), 50–56.
Xu, S.L., Zhu, Y.Z., Cai, Y.Q., Sun, H.L., Cao, H.T., Shi, J.Q., 2022. Predicting the permeability coefficient of polydispersed sand via coupled CFD–DEM simulations. Comput. Geotech. 144, 104634.
Zhang, F.S., Wang, T., Liu, F., Peng, M., Furtney, J., Zhang, L.M., 2020. Modeling of fluid-particle interaction by coupling the discrete element method with a dynamic fluid mesh: Implications to suffusion in gap-graded soils. Comput. Geotech. 124, 103617.
Zhu, H.P., Yu, A.B., 2003. The effects of wall and rolling resistance on the couple stress of granular materials in vertical flow. Physica A 325 (3–4), 347–360.